16th World Congress in Computational Mechanics (WCCM)
21-26 July 2024, Vancouver, Canada
A. Korobenko, M. Laforest, S. Prudhomme, R. Vaziri (Eds)

INFLUENCE EVALUATION OF FLOW DIVERTER STENT PARENT VESSEL COVERAGE ON CEREBRAL ANEURYSM THROUGH THE CFD-DEM COUPLING SIMULATION

YOSHIO OHKURA[1], DAI WATANABE[2],
RYO TANIGUCHI[3], SOICHIRO YAMANI[4] AND HIROYUKI TAKAO[5]

[1]Shibaura Institute of Technology Graduate School
307 Fukasaku, Saitama City, Saitama 337-8570, Japan
nb22106@shibaura-it.ac.jp

[2]Shibaura Institute of Technology Graduate School
307 Fukasaku, Saitama City, Saitama 337-8570, Japan
dai-wata@shibaura-it.ac.jp

[3]Shibaura Institute of Technology Graduate School
307 Fukasaku, Saitama City, Saitama 337-8570, Japan
bq20089@shibaura-it.ac.jp

[4]Shibaura Institute of Technology Graduate School
307 Fukasaku, Saitama City, Saitama 337-8570, Japan
bq20088@shibaura-it.ac.jp

[5]The Jikei University School of Medicine
3-25-8 Nishi-Shimbashi, Minato-ku, Tokyo 105-8461, Japan
hitakao821takao@gmail.com

Key words: Cerebral aneurysm, Flow diverter, Stent, FEM, PFEM-2, DEM.

Abstract. Cerebral aneurysms are a type of cerebrovascular disorder where a balloon-like bulge forms in part of an artery in the brain. One of the developed treatments for large cerebral aneurysms is the Flow-diverter Stent (FDS) placement technique. Effective treatment outcomes in cerebral aneurysm treatment using FDS require proper placement of the device. Improper placement can lead to increased blood flow velocity and Wall Shear Stress (WSS) within the aneurysm, as well as increased pressure, which suggests a potential risk of rupture in large aneurysms. Considering these circumstances, this study evaluates the impact of FDS positioning on cerebral aneurysms by creating multiple FDS placement models with the device positioned proximally and distally to the aneurysm. Subsequently, we conducted fluid-structure interaction simulation analyses using the Particle Finite Element Method-Second Generation (PFEM-2) for the non-Newtonian fluid model of blood and the Discrete Element Method (DEM) for the FDS. This study reports the results of comparing blood behavior, WSS, and pressure inside the cerebral aneurysm based on the FDS placement position.

1 INTRODUCTION

Cerebral aneurysms refer to conditions where a balloon-like bulge forms in part of an artery in the brain, commonly seen in women aged 40 to 60, and is a type of cerebrovascular disorder. The exact cause is not fully understood, but it is believed to form due to congenital defects in the arterial wall's medial layer, combined with acquired factors such as hypertension, arteriosclerosis, smoking, genetic predisposition, and endothelial repair impairment. These aneurysms are thinner and more fragile compared to normal vessels [1]. If a cerebral aneurysm ruptures, it causes subarachnoid hemorrhage, with a low societal reintegration rate of about 30% for affected individuals. Therefore, surgical treatment is sometimes performed before rupture.

One of the developed treatments for large cerebral aneurysms is the Flow-diverter Stent (FDS) placement technique [2,3,4]. This technique involves using a cylindrical device, known as FDS, made of finely woven metal wires in a mesh pattern. The device is placed in the cerebral artery to cover the neck of the aneurysm using a catheter. Due to its high metal density, the FDS reduces blood flow into the aneurysm, promoting thrombosis and preventing rupture.

Effective treatment outcomes in cerebral aneurysm treatment using FDS require proper placement of the device. Nakayama et al. reported that, based on Computational Fluid Dynamics (CFD) analysis, certain strand patterns increased the flow velocity and Wall Shear Stress (WSS) within the aneurysm by 13%, highlighting a potential link to delayed aneurysm rupture post-FDS placement [5]. Cebral et al. confirmed through CFD analysis that FDS placement increased pressure within the aneurysm, suggesting a risk of rupture in large aneurysms [6]. Ma et al. reported a correlation between the increased metal coverage rate of FDS over the aneurysm neck and reduced flow velocity based on CFD analysis using structural analysis results after FDS placement [7,8].

Considering these circumstances, this study focuses on the placement position of the FDS. To evaluate the impact of FDS positioning on cerebral aneurysms, we created multiple FDS placement models with the device positioned proximally and distally to the aneurysm. Subsequently, we conducted fluid-structure interaction simulation analyses using the Particle Finite Element Method-Second Generation (PFEM-2) for the non-Newtonian fluid model of blood and the Discrete Element Method (DEM) for the FDS. This study reports the results of comparing blood behavior, flow velocity, pressure, and WSS inside the cerebral aneurysm based on the FDS placement position.

2 METHODS

The analysis flow is shown in Figure 1. A Finite Element Method (FEM) deployment analysis of the FDS was performed using a beam element model created by combining vascular structures generated from DICOM (Digital Imaging and Communications in Medicine) data and functions. The shape of the FDS beam element model after deployment was divided to create FDS shapes with the same conditions at three different positions. Subsequently, the nodes of the beam elements were interpolated and converted into DEM particles. This converted DEM particle model FDS, along with the PFEM-2, was used for coupled analysis to evaluate the impact on cerebral aneurysms.

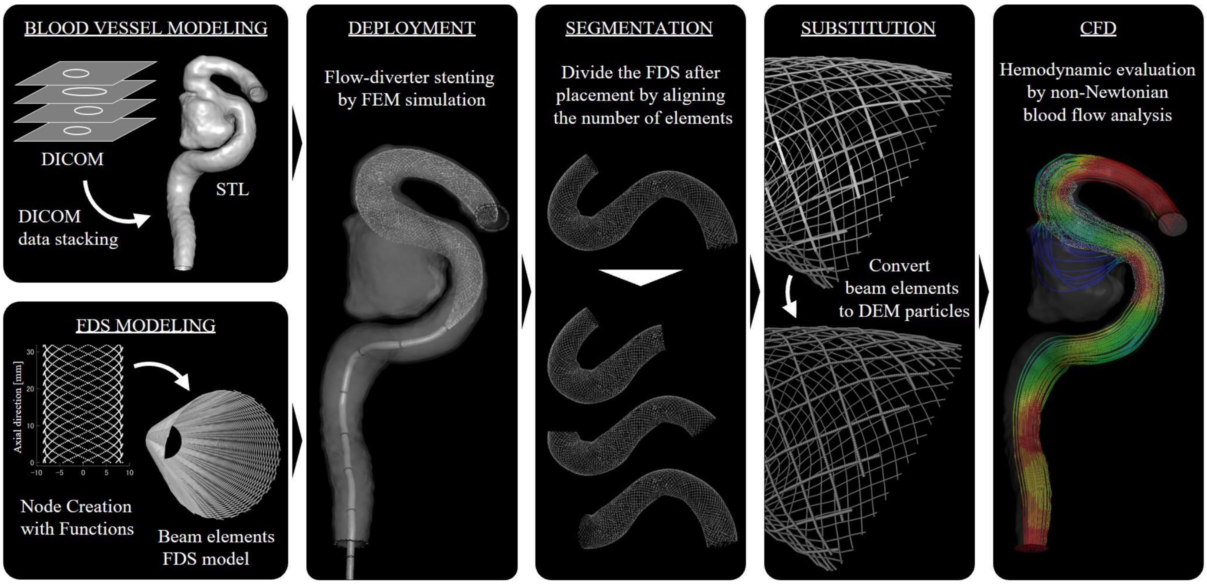

Figure 1: Flow of FDS deployment analysis and blood flow analysis.

2.1 Governing equations [9,10]

The CFD method used was PFEM-2. PFEM-2 is aimed at solving the incompressible Navier-Stokes equations. The conservation of momentum and mass is represented by the Navier-Stokes equation (1) and the continuity equation (2):

$$\rho\left(\frac{du_i}{dt}+u_j\frac{\partial u_i}{\partial x_j}\right) = \frac{\partial \sigma_{i,j}}{\partial x_j}+\rho f_i \tag{1}$$

$$\frac{\partial u_i}{\partial x_i}=0 \tag{2}$$

Here, u denotes the velocity, p the pressure, ρ the density, and f_i the body force. The total stress tensor is expressed by the equation (3):

$$\sigma_{ij}=-p\delta_{ij}+\mu\left(\frac{\partial u_i}{\partial x_j}+\frac{\partial u_j}{\partial x_i}-\frac{2}{3}\frac{\partial u_l}{\partial x_l}\delta_{ij}\right) \tag{3}$$

Where is μ the dynamic viscosity coefficient and δ_{ij} is the Kronecker delta. Assuming the fluid is incompressible, the total stress tensor is simplified by equation (4):

$$\sigma_{ij}\approx -p\delta_{ij}+\mu\left(\frac{\partial u_i}{\partial x_j}+\frac{\partial u_j}{\partial x_i}\right) \tag{4}$$

Similarly, $\partial\sigma_{ij}/\partial x_j$ can be expressed as equation (5):

$$\frac{\partial \sigma_{ij}}{\partial x_j}=-\frac{\partial p}{\partial x_j}\delta_{ij}+\frac{\partial}{\partial x_j}\left[\mu\left(\frac{\partial u_i}{\partial x_j}+\frac{\partial u_j}{\partial x_i}\right)\right] \tag{5}$$

For near-incompressible flows, this can be further simplified as equation (6):

$$\frac{\partial \sigma_{ij}}{\partial x_j} \approx -\frac{\partial p}{\partial x_j}\delta_{ij} + \mu \frac{\partial}{\partial x_j}\left(\frac{\partial u_i}{\partial x_j}\right) \tag{6}$$

From these, the governing equations obtained are equations (7) and (8):

$$\rho\left(\frac{du_i}{dt} + u_j \frac{\partial u_i}{\partial x_j}\right) = -\frac{\partial p}{\partial x_i} + \mu \frac{\partial^2 u_i}{\partial x_j \partial x_j} + \rho f_i \tag{7}$$

$$\frac{\partial u_i}{\partial x_i} = 0 \tag{8}$$

2.2 Three step fractional method [9,10]

The Three Step Fractional Method solves the Navier-Stokes equations efficiently by separating the velocity and pressure fields into the following three steps, as shown in equations (7) and (8).

Step 1: Predict the velocity field. The predicted velocity u_i^*, excluding the pressure term, is calculated as shown in equation (9)

$$u_i^* = u_i^n - \gamma \frac{\Delta t}{\rho}\frac{\partial p^n}{\partial x_i}\delta_{ij} + \frac{\Delta t}{\rho}\mu \frac{\partial^2 u_i^{n+\theta}}{\partial x_j \partial x_j} - \Delta t u_j^{n+\theta}\frac{\partial u_i^{n+\theta}}{\partial x_i} + \Delta t f_i \tag{9}$$

Here, γ is a correction coefficient and θ represents the time integration scheme parameter.

Step 2: Update the Pressure Field. Next, the pressure field p^{n+1} is calculated using the incompressibility condition. Applying the continuity equation results in the pressure Poisson equation (10):

$$\frac{\partial}{\partial x_i}\left(u_i^{n+1} - u_i^*\right) = \frac{\Delta t}{\rho}\frac{\partial}{\partial x_i}\frac{\partial}{\partial x_i}\left(-p^{n+1} + \gamma p^n\right)\delta_{ij} \tag{10}$$

From this equation, the first term on the left-hand side vanishes:

$$\frac{\partial}{\partial x_i}\left(-u_i^*\right) = \frac{\Delta t}{\rho}\frac{\partial}{\partial x_i}\frac{\partial}{\partial x_i}\left(-p^{n+1} + \gamma p^n\right)\delta_{ij} \tag{11}$$

The next step pressure is determined from equation (11) and the boundary conditions.

Step 3: Update the Velocity Field. Finally, the velocity field u_i^{n+1} is updated using the computed pressure:

$$u_i^{n+1} = u_i^* + \frac{\Delta t}{\rho}\frac{\partial}{\partial x_i}\left(-p^{n+1} + \gamma p^n\right)\delta_{ij} \tag{12}$$

In this manner, the computation maintains the incompressible flow condition while ensuring coordination between the velocity and pressure fields.

2.3 Governing equation of structure [11]

DEM was proposed by Cundall et al. to represent particles such as granules and powders [12]. In this study, these DEM particles are fixed in space, and the translation and rotation of individual particles are completely constrained. Therefore, only the boundaries are considered, and the explanation is omitted. The boundaries are coupled by transferring the drag force f_d as shown in equation (13).

$$f_d = \frac{1}{2} v_f^2 A \rho_f C_d \tag{13}$$

Here, v_f denotes the velocity, A the projected area, ρ_f the fluid density, and C_d the drag coefficient.

2.4 Blood vessels and blood modeling

The vessels were modeled by stacking DICOM data measured from patients, creating smoothed three-dimensional STL data. Subsequently, remeshing and thickening were performed to create an FEM model for simulation purposes. The constructed vessel is shown in Figure 2. Table 1 shows the material model, element type, and number of elements used.

Blood is a shear-thinning fluid that depends on shear rate. Therefore, the Carreau model was used to represent the behavior of blood. The apparent viscosity coefficient using the Carreau model is shown in equation (14):

$$\mu_{(\dot{\gamma})} = \mu_\infty + (\mu_0 - \mu_\infty)\left[1 + \{\dot{\gamma}\lambda\}^2\right]^{\frac{n-1}{2}} \tag{14}$$

Here, $\dot{\gamma}$ denotes the shear rate, and following Cho et al., the zero-shear viscosity μ_0 is set to 5.60×10^{-2} Pa · s, the infinite-shear viscosity μ_∞ to 3.45×10^{-3} Pa · s, the time constant λ to 3.313 sec, and the exponent n to 0.3568 [13]. Additionally, following Ma et al., the blood density is set to 1056 kg/m^3 [8]. The results reflecting these constants are shown in Figure 3.

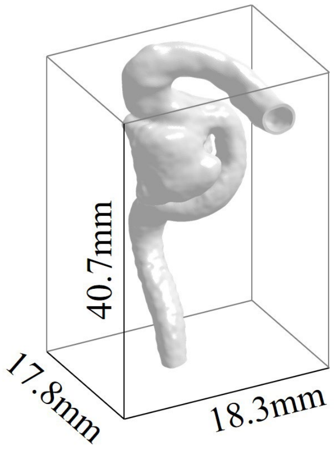

Figure 2: Blood vessel FE model.

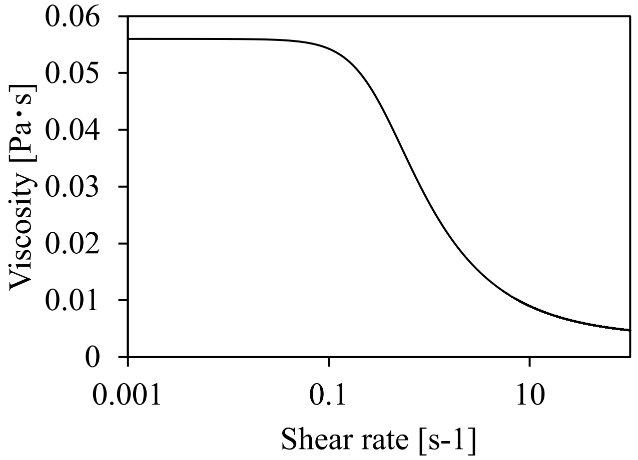

Figure 3: Relationship between shear rate and viscosity coefficient.

Table 1: Model information and physical properties of finite element models [7,13].

Model and Unit		36 strands / 12 strands	Crimper	Catheter	Blood vessel
Material model	[・]	Elastic	Elastic	Elastic	Rigid
Element Model	[・]	Beam	Shell	Shell / Solid	Solid
Number of elements	[elements]	6784 / 3392	320	21600 / 1200	80358
Density	[kg/m3]	8250 / 21340	233000	7000	-
Young's modulus	[Pa]	2.3 x 1011	5.0 x 104	3.0 x 109	-
Poisson's ratio	[・]	0.30 / 0.40	0.17	0.30	-

2.5 Flow-diverter stent and catheter modeling

The FDS was modeled as a self-expanding braided stent composed of 48 interwoven wires. To simplify the modeling process, a braiding function was created to replicate the interweaving without the actual braiding process. The design variables of the FDS are shown in Figure 4. Table 1 shows the material model, element type, number of elements, and material properties used. The material model was set as a linear elastic body for shape comparison after placement, and Hughes-Liu beam elements were used to balance computational cost. The FDS consists of 36 strands of Co-Ni-Cr-Mo alloy and 12 strands of Pt-W alloy. Based on the material properties referenced from Ma et al. and Otomo et al., two types of wires with different materials were replicated in one model [7,14]. Additionally, the friction coefficients used between the models are shown in Table 2.

For the catheter, considering the computational cost, the guide wire and delivery wire used for FDS placement were omitted, and only the microcatheter was replicated. Therefore, the insertion support of the microcatheter by the guide wire and the fixation of the BS by the delivery wire were replicated by forced displacement. The design variables of the microcatheter model are shown in Figure 5. Table 1 shows the material model, element type, number of elements, and material properties used. The material model was set as a linear elastic body, and the modeling was performed using fully integrated shell elements and one-point integrated solid elements.

2.6 FDS packaging

The naturally created FDS needs to be packaged into the microcatheter. Therefore, a cylinder was created to compress the FDS, as shown in Figure 5. The compression process of the FDS is also shown in Figure 5. By compressing the cylinder inward through forced displacement, the FDS was also compressed. The compression continued until the FDS was reduced to a size that could be packaged into the microcatheter, and the entire assembly was restrained to prevent the FDS from re-expanding after compression. The FDS was then packaged into the microcatheter while maintaining this restrained state. After being packaged into the microcatheter, the FDS was released.

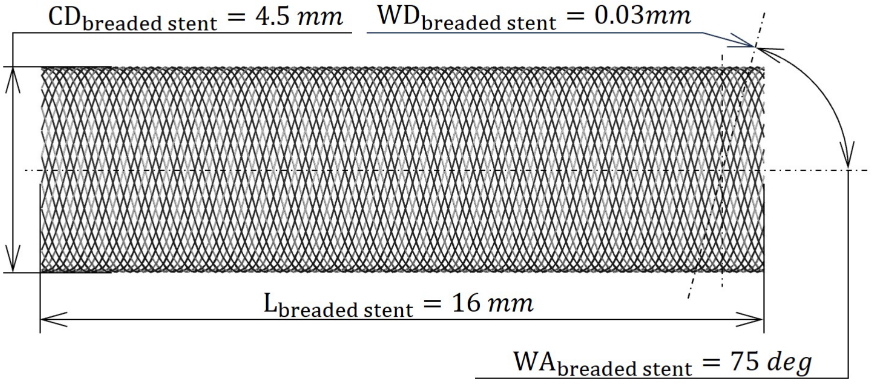

Figure 4: Braiding and design variables of FDS.

Table 2: Static and dynamic friction coefficient conditions between finite element models [13].

Static Friction / Dynamic Friction	FDS	Crimper	Catheter	Blood vessel
FDS	0.05 / 0.01	0.03 / 0.01	0.05 / 0.01	0.08 / 0.04
Crimper	0.03 / 0.01	-	-	-
Catheter	0.05 / 0.01	-	-	-
Blood vessel	0.08 / 0.04	-	-	-

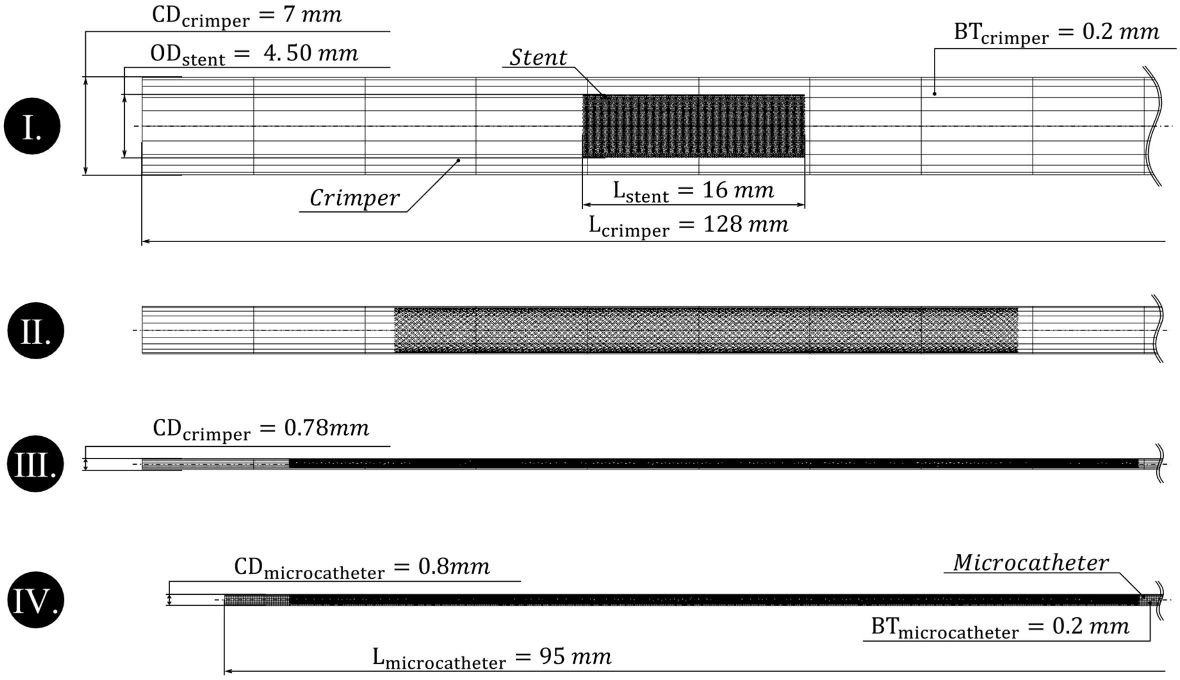

Figure 5: FDS packaging process. The process was divided into stages I to IV. The FDS is compressed to a size smaller than the catheter using a crimper. Next, the crimper is removed and replaced with the catheter.

2.7 Deployment analysis

Structural analysis using FEM was conducted through dynamic analysis with ANSYS LS-DYNA R14.1 (ANSYS Inc., Canonsburg, PA). The explicit method was used for time discretization due to the nonlinear contact expected from the FDS. The central difference method was employed in the explicit method, and the time increment during analysis was set to 0.9 times the automatically calculated time increment by ANSYS LS-DYNA. For deployment, the packaged FDS and the microcatheter were inserted into the blood vessel by applying forced displacement. During deployment, the microcatheter was given a forced displacement in the opposite direction of insertion, and simultaneously, the proximal end of the FDS was displaced distally by a virtual pusher to simulate FDS deployment. The deployment process is shown in Figure 6.

2.8 Model Remaking and Mesh Conversion

To evaluate the impact of the FDS placement position on a cerebral aneurysm, the deployed beam element model of the FDS was divided and remade into three models: an FDS placed proximally to the aneurysm, an FDS placed centrally, and an FDS placed distally. The division was performed so that the number of elements remained equal. The remade beam element models were then converted into DEM particles for coupled analysis using PFEM-2 and DEM. The nodes between the placed FDS shapes were interpolated and converted into DEM particles. The number of particles after interpolation was 87168, with an inter-particle distance of 0.02 mm.

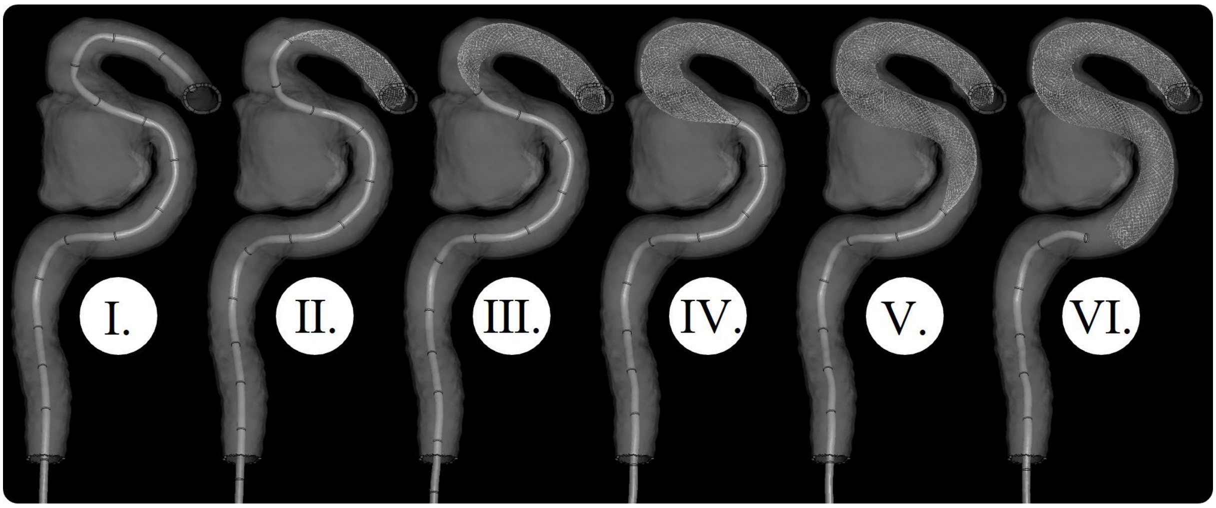

Figure 6: FDS Deployment analysis results.

2.9 Blood Flow Analysis

For the four models three models with remade FDS placement positions and one model without FDS a one-way fluid-structure interaction analysis from structure to fluid using PFEM-2 and DEM was conducted with ANSYS LS-DYNA R14.1 (ANSYS Inc., Canonsburg, PA). The FDS converted into DEM particles was fully constrained in space. Additionally, computational cost was reduced by not performing contact calculations between particles. Table 0 shows the papers that report the blood flow velocity in the internal carotid artery. The maximum flow velocity in peak systolic flow velocity (PSV) is approximately 0.8 m/sec at its highest. Based on this, a steady inflow velocity of 0.8 m/sec was applied as the inflow condition. A pressure condition of 0 Pa was applied to the outflow condition. The fluid mesh consisted of approximately 9.6 million elements. A no-slip condition was applied to the vessel wall, with the boundary layer consisting of 10 layers.

Table 3: Papers on the blood flow velocity and diameter of the internal carotid artery [14,15,16,17,18,19]. To determine the blood flow velocity, multiple papers on blood flow velocity were compared.

Reference number	Measured vascular site	Blood flow velocity [m/sec]			Vascular diameter [mm]	Age	Remarks column
		Maximum	Minimum	Average			
[15]	ICA	0.480	0.160	-	4.44 ± 0.56	24-83	Retrieved from graph
[16]	ICA	0.626	0.380	-	-	24	-
	ICA	0.614	0.378	-	-	23	-
[17]	ICA-C1	-	-	0.25 ± 0.052	-	46.2 ± 13 (20-70)	-
	ICA-C3	-	-	0.25 ± 0.069	-	46.2 ± 13 (20-70)	-
	ICA-C7	-	-	0.35 ± 0.100	-	46.2 ± 13 (20-70)	-
	ICA-C1	-	-	0.26 ± 0.059	-	46.2 ± 13 (20-70)	-
	ICA-C3	-	-	0.25 ± 0.250	-	46.2 ± 13 (20-70)	-
	ICA-C7	-	-	0.35 ± 0.100	-	46.2 ± 13 (20-70)	-
	ICA-C1	0.323	0.112	-	-	46.2 ± 13 (20-70)	Retrieved from graph
	ICA-C3	0.435	0.202	-	-	46.2 ± 13 (20-70)	Retrieved from graph
	ICA-C7	0.548	0.190	-	-	46.2 ± 13 (20-70)	Retrieved from graph
[18]	ICA	0.525 ± 0.085	-	-	-	27.7 ± 3.9	-
	ICA	0.598 ± 0.085	-	-	-	27.7 ± 3.9	-
	ICA	0.830 ± 0.143	-	-	-	27.7 ± 3.9	-
	ICA	0.768 ± 0.139	-	-	-	27.7 ± 3.9	-
	ICA	-	0.217 ± 0.038	-	-	27.7 ± 3.9	-
	ICA	-	0.256 ± 0.043	-	-	27.7 ± 3.9	-
	ICA	-	0.299 ± 0.052	-	-	27.7 ± 3.9	-
	ICA	-	0.329 ± 0.072	-	-	27.7 ± 3.9	-
[19]	ICA	0.373 ± 0.026	-	0.108 ± 0.021	5.6	-	-
	ICA	0.369 ± 0.013	-	0.083 ± 0.016	5.6	-	-
[20]	ICA	0.82 (0.50-1.12)	0.34 (0.21-0.45)	-	-	20-39	-
	ICA	0.76 (0.60-1.01)	0.31 (0.24-0.40)	-	-	40-49	-
	ICA	0.80 (0.59-0.96)	0.34 (0.22-0.44)	-	-	50-59	-
	ICA	0.79 (0.62-1.09)	0.28 (0.19-0.38)	-	-	60-69	-
	ICA	0.71 (0.40-0.97)	0.26 (0.11-0.37)	-	-	70-79	-
	ICA	0.76 (0.56-0.98)	0.18 (0.11-0.22)	-	-	80-	-

3 RESULTS

From the results of the blood flow analysis, it was observed that in the cerebral aneurysm without FDS placement, blood flow generated vortices within the aneurysm. In contrast, the three models with FDS placement showed a reduction in vortices within the aneurysm. Regarding blood flow velocity, the three models with FDS placement exhibited an increase in the region showing velocities above 0.8 m/sec at the base of the aneurysm. Among these, the model with the FDS placed proximally showed the greatest increase in the region with velocities above 0.8 m/sec. In inverse proportion to this phenomenon, the model with the FDS placed proximally showed lower blood flow pressure near the aneurysm wall compared to the other models with FDS placement, while the model with the FDS placed distally exhibited higher blood flow pressure. There was a noticeable difference in wall shear stress at the neck of the aneurysm between the models with and without FDS placement, with the model with the proximally placed FDS showing higher regions of wall shear stress near the aneurysm wall.

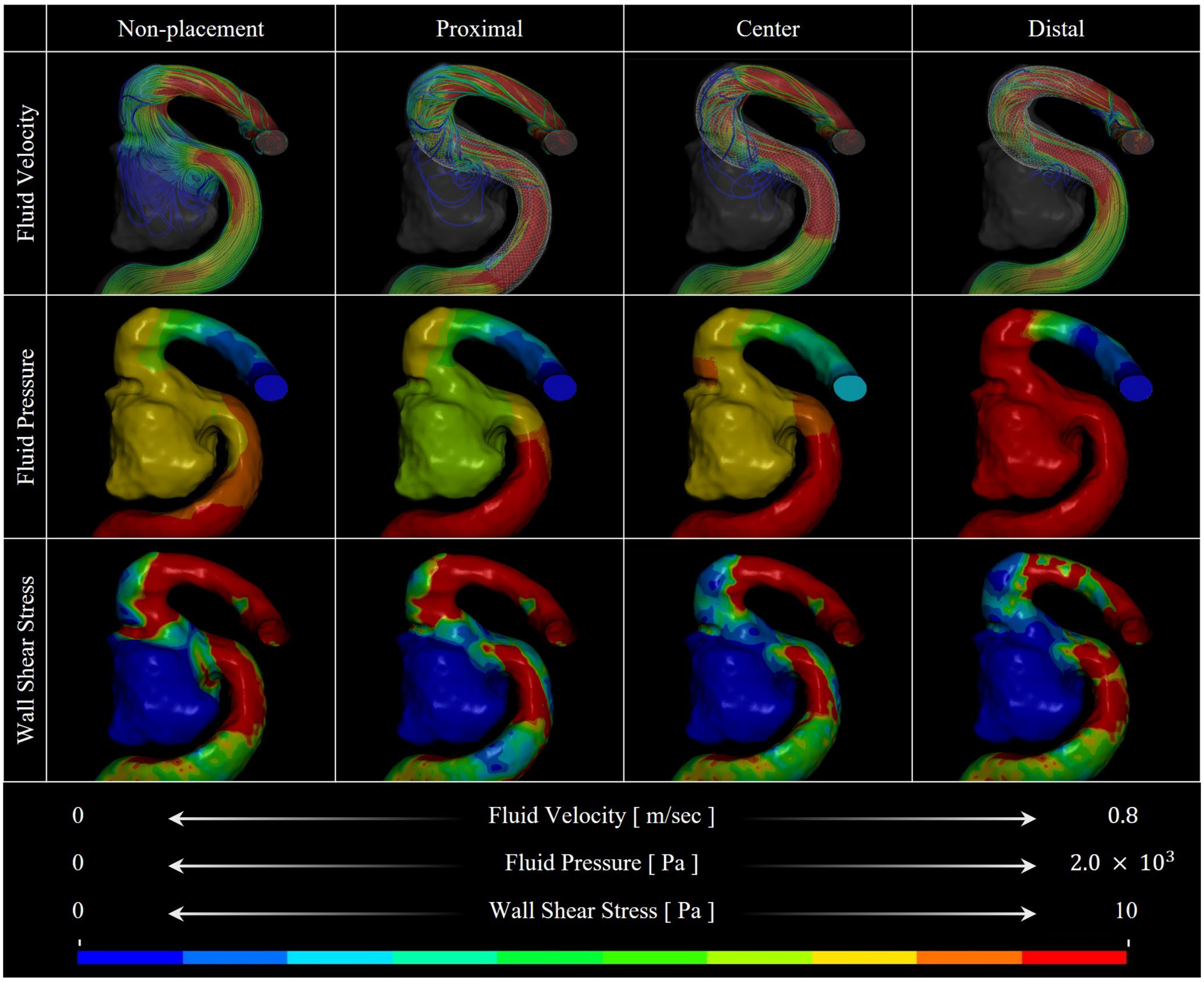

Figure 6: Blood Flow Analysis Results. The analysis compared three types of parameters WSS, fluid velocity, and fluid pressure for different scenarios: without FDS, FDS placed proximally to the cerebral aneurysm, FDS placed centrally, and FDS placed distally.

4 DISCUSSION

An increase in blood flow velocity was observed with the placement of the FDS. This is thought to be due to the reduction in vessel diameter caused by the FDS, which increased the blood flow velocity. According to Bernoulli's theorem, the relationship between velocity and static pressure explains why the model with the FDS placed proximally showed a decrease in pressure, while the model with the FDS placed distally showed an increase in pressure. This pressure change is expected to be related to the vortices generated within the cerebral aneurysm. It can be understood that when the altered fluid pressure is continuously connected from within the cerebral aneurysm to the distal end without an increase in pressure, it leads to a reduction in vortices generated within the flow. These results suggest that the placement position of the FDS, even with equal metal coverage rates, may affect the occlusiveness of the treatment outcome. Regarding the impact on WSS, the difference might not be apparent due to the analysis time and the steady inflow boundary conditions applied.

5 CONCLUSION

This study evaluated the behavior of blood flow, pressure, and WSS based on differences in the placement position of the FDS through deployment analysis and blood flow analysis. It was confirmed that the placement of the FDS increased the blood flow velocity in the parent vessel, leading to changes in fluid pressure. By utilizing this phenomenon, it is possible to intentionally reduce the pressure within the cerebral aneurysm. Additionally, it was observed that a continuous decrease in fluid pressure towards the distal end could reduce vortices within the cerebral aneurysm after FDS placement. These results suggest that the placement position of the FDS, even with equal metal coverage rates, may affect the occlusiveness of the treatment outcome. Further validation is needed to substantiate these findings.

REFERENCES

[1] Yutaka Okaniwa, Neurology and Neurosurgery, Medic Media, Vol. 1, (2011) **7**:106-121.

[2] Pedro Lylyk, Carlos Miranda, Rosana Ceratto, Angel Ferrario, Esteban Scrivano, Hugh Ramirez Luna, Aaron L Berez, Quang Tran, Peter K Nelson and David Fiorella, Curative endovascular reconstruction of cerebral aneurysms with the pipeline embolization device: The Buenos Aires experience, Neurosurgery, Vol. 64, (2009) **4**:632-642.

[3] I. Szikora, Z. Berentei, Z. Kulcsar, M. Marosfoi, Z.S. Vajda, W. Lee, A. Berez and P.K. Nelson, Treatment of intracranial aneurysms by functional reconstruction of the parent artery: the Budapest experience with the pipeline embolization device, American journal of Neuroradiology, Vol. 31, (2010) **6**:1139-1147.

[4] Murat Velioglu, Osman Kizilkilic, Hakan Selcuk, Burak Kocak, Ercan Tureci, Civan Islak and Naci Kocer, Early and midterm results of complex cerebral aneurysms treated with Silk stent, Neurosurgery, Vol. 54, (2012) **12**:1355-1365.

[5] Toshio Nakayama and Makoto Ohta, Several stent struts increase blood flow speed in cerebral aneurysm, The 5th International Stent Symposium, (2008) 27.

[6] J.R. Cebral, F. Mut, M. Raschi, E. Scrivano, R. Ceratto, P. Lylyk, and C.M. Putman, Aneurysm Rupture Following Treatment with Flow-Diverting Stents: Computational Hemodynamics Analysis of Treatment, American journal of neuroradiology, Vol. 32, (2011) **1**:27-33.

[7] Ding Ma, Gary F. Dargush, Sabareesh K. Natarajan, Elad I. Levy, Adnan H. Siddiqui, Hui Meng, Computer modeling of deployment and mechanical expansion of neurovascular flow diverter in patient-specific intracranial aneurysms, Vol. 45, (2012) **13**:2256-2263.

[8] D. Ma, J. Xiang, H. Choi, T.M. Dumont, S.K. Natarajan, A.H. Siddiqui, H. Meng, Enhanced aneurysmal flow diversion using a dynamic push-pull technique: an experimental and modeling study, American Journal of Neuroradiology, Vol. 35, (2014) **9**:1779-1785.

[9] Facundo Del Pin, Sergio Idelsohn, Eugenio Oñate, Romain Aubry, The ALE/Lagrangian Particle Finite Element Method: A new approach to computation of free-surface flows and fluid–object interactions, Computers & fluids, Vol. 36, (2007) 1:27-38.

[10] LSTC, ICFD THEORY MANUAL, (2014) 4-9.

[11] Pär Jonsén, Samuel Hammarberg, Bertil I. Pålsson, Göran Lindkvist, Preliminary validation of a new way to model physical interactions between pulp, charge and mill structure in tumbling mills, Minerals Engineering, Vol. 130, (2019) 76-84.

[12] P.A. Cundall and O. D. L. Strack, A discrete numerical model for granular assemblies, Geotechnique, Vol.29, (1979) 1:47-65.

[13] Y.I. Cho and K.R. Kensey, Effects of the non-Newtonian viscosity of blood on flows in a diseased arterial vessel. Part 1: steady flows", Biorheology, Vol. 28, (1991) 241-262.

[14] Takuma Otomo, Hiroaki Matsumoto, Naoyuki Nomura and Akihiko Chiba, Influence of cold-working and subsequent heat-treatment on young's modulus and strength of co-ni-cr-mo alloy, Journal of Materials Transactions, Vol.51, (2010) **3**:434-441.

[15] Patrick M. McGah, Michael R. Levitt, Michael C. Barbour, Ryan P. Morton, John D. Nerva, Pierre D. Mourad, Basavaraj V. Ghodke, Danial K. Hallam, Laligam N. Sekhar, Louis J. Kim and Alberto Aliseda, Accuracy of Computational Cerebral Aneurysm Hemodynamics Using Patient-Specific Endovascular Measurements, Annals of Biomedical Engineering, Vol. 42, (2014) **3**:503-514.

[16] Sole Lindvåg Lie, Jonny Hisdal and Lars Øivind Høiseth, Cerebral blood flow velocity during simultaneous changes in mean arterial pressure and cardiac output in healthy volunteers, European Journal of Applied Physiology, Vol. 121, (2021) **8**:2207-2217.

[17] Rick J. van Tuijl, Ynte M. Ruigrok, Birgitta K. Velthuis, Irene C. van der Schaaf, Gabriël J. E. Rinkel and Jaco J. M. Zwanenburg, Velocity Pulsatility and Arterial Distensibility Along the Internal Carotid Artery, Journal of the American Heart Association, Vol. 9, (2020) **16**:10.1161/JAHA.120.016883.

[18] Ilko L. Maier, Sabine Hofer, Arun A. Joseph, K. Dietmar Merboldt, Zhengguo Tan, Katharina Schregel, Michael Knauth, Mathias Bähr, Marios-Nikos Psychogios, Jan Liman and Jens Frahm, Carotid artery flow as determined by real-time phase-contrast flow MRI and neurovascular ultrasound: A comparative study of healthy subjects, European Journal of Radiology, Vol. 106, (2018) 38-45.

[19] Anderson Chun On Tsang, Simon Sui Man Lai, Wai Choi Chung, Abraham Yik Sau Tang, Gilberto Ka Kit Leung, Alexander Kai Kei Poon, Alfred Cheuk Hang Yu, and Kwok Wing Chow, Blood flow in intracranial aneurysms treated with Pipeline embolization devices: computational simulation and verification with Doppler ultrasonography on phantom models, Ultrasonography, Vol. 34, (2015) **2**:98-108.

[20] Y Nagai, M K Kemper, C J Earley, E J Metter, Blood-flow velocities and their relationships in carotid and middle cerebral arteries, Ultrasound Med Biol, Vol. 24, (1998) **8**:1131-1136.